



30 months dataset of glider physico-chemical data off Mayotte Island near the Fani Maoré volcano

Alexandre Heumann^{1,2}, Félix Margirier¹, Emmanuel Rinnert², Pascale Lherminier³, Carla Scalabrin², Louis Géli², Orens Pasqueron de Formmervault⁴, and Laurent Béguey¹

¹ALSEAMAR, Rousset, France

²Geo-Ocean UMR 6538 CNRS - Ifremer - UBO, Plouzané, France

³LOPS UMR 6523 CNRS - Ifremer - UBO - IRD, Plouzané, France

⁴OceanOPS, World Meteorological Organization / Intergovernmental Oceanographic Commission (IOC) of UNESCO, Monaco

Correspondence: Alexandre Heumann (aheumann@alseamar-alcen.com)

Abstract. In May 2018, an unprecedented long and intense seismic-volcanic crisis broke out off the island of Mayotte (Indian Ocean) and was associated with the birth of an underwater volcano (Fani Maoré). Since then, an integrated observation network has been created (REVOSIMA), with the given objective of monitoring and better understanding underwater volcanic phenomena. Recently, an unmanned submarine glider (SeaExplorer glider) has been deployed to supplement the data obtained during a series of oceanographic surveys (MAYOBS) carried out on an annual basis. Operated by ALSEAMAR, the glider performed a continuous monitoring of 30 months of the water column from the sea surface to 1250 meters water depth with the objective to acquire hydrological properties, water currents and dissolved gas concentrations. This monitoring already showed that it is feasible and valuable to measure autonomously, continuously and at a high spatio-temporal scale, physical (temperature, salinity, ocean current) and biogeochemical parameters (O_2 , CH_4 , CO_2 , bubbles/droplets, vertical speeds anomalies related to droplets) over several months from a glider. In particular, innovating sensing capabilities (e.g., MINICO2, ADCP) have shown a great potential in the context of the Mayotte seismic volcano crisis, despite technical challenges (complex algorithms, sensor capabilities, etc.).

1 Introduction

Mayotte is a french overseas department, part of the volcanic archipelago of the Comoros Islands, northwest of Madagascar. It was last volcanically active on land less than 7,000 years ago (Zinke *et al.*, 2003; 2005).

On May 10, 2018, a seismic-volcanic crisis of unprecedented intensity and duration began off the two main islands of Grande-Terre and Petite-Terre (Lemoine *et al.*, 2020). More than 11,000 earthquakes were recorded, up to a magnitude of 5.9, in an area where only two seismic events had been recorded since 1972 (Feuillet *et al.*, 2021). At sea, the epicenters of these earthquakes were divided into the Proximal area (5 to 15 km east of Petite-Terre) and Distal area (25 km east of Petite-Terre).

Following the start of this seismic crisis on July 1, 2018, surface displacements were measured by the GPS stations present in Mayotte, revealing an eastward displacement of between 21 and 25 cm for all these stations, as well as a subsidence of between

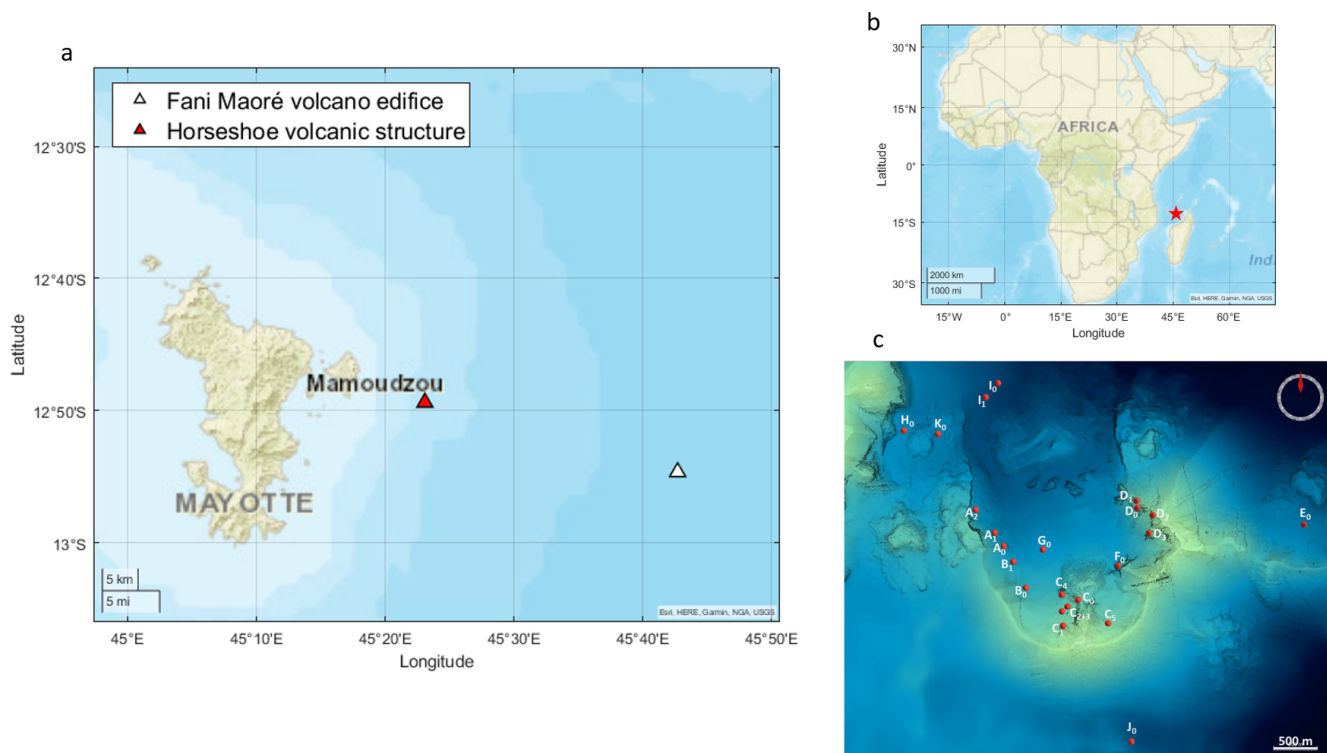


Figure 1. Map view of Mayotte (a); the Fani Maoré volcano edifice is represented by the white triangle which lies 50 km southeast of Mayotte and the Horseshoe area is represented by the red triangle located 10 km east of Mayotte. Map view of Africa and Middle East (b) where the red triangle is the Mayotte island. Map illustrating the bathymetry of the Horseshoe structure (c). The red dots correspond to the discovered emission sites of magmatic fluid identified with the multibeam echosounder during the REVOSIMA MAYOBS cruises (<https://doi.org/10.12770/070818f6-6520-49e4-bafd-9d4d0609bf7d>) and validated by in situ visual observations with the ROV VICTOR during the GEOFLAMME cruise (DOI 10.17600/18001297). Bathymetric data were provided with a resolution of 20 m (<https://doi.org/10.18142/291>).

10 and 19 cm depending on their location (Feuillet *et al.*, 2021).

In response to this crisis, French laboratories and institutions (IPGP/CNRS/BRGM/IFREMER/IPGS) created a volcanological and seismological monitoring network in Mayotte, the REVOSIMA <http://www.ipgp.fr/fr/revosima/acteurs-reseau>. This observatory, both marine and terrestrial, benefits from the financial support of several ministries (Ministry of Overseas, Ministry of the Interior, Ministry of Higher Education, Research and Innovation, Ministry of Ecological Transition and Solidarity) and aims to further our understanding of the seismic-volcanic activity for preservatives measures in order to protect populations. As part of REVOSIMA, several oceanographic cruises have been carried out (MAYOBS cruises, <https://doi.org/10.18142/291>) and bulletins monitoring seismo-volcanic activity are published monthly (<http://www.ipgp.fr/fr/revosima/actualites-reseau>). The first oceanographic cruise (MAYOBS1) was carried out from May 02 to 18, 2019 on the RV *Marion Dufresne*, and led to the discovery of the brand new Fani Maoré submarine eruptive volcano. A new volcanic structure formed during this crisis



around 800 m high, located 50 km off the coast of Mayotte, at a depth of 3,500 meters below sea surface (mbss, Feuillet *et al.*, 2021, Aiken *et al.*, 2021, Fig. 1). The estimated volume of magma emitted during this eruptive period is 6.55 km^3 , ranking this event as the largest submarine volcanic eruption ever documented (Feuillet *et al.*, 2021). Other lava flows were revealed during
35 subsequent oceanographic cruises, revealing the presence of four other lava outlets in the nearby area around the new volcano (Feuillet *et al.*, 2021.). During the MAYOBS cruises, the Horseshoe preexisting volcanic structure, located above the Proximal swarm at an average seafloor depth of 1,400 mbss, was a particular area of interest (Fig. 1). Acoustic plumes and geochemical anomalies (elevated concentrations of dissolved gases such as carbon dioxide CO_2 , methane CH_4 and dihydrogen H_2) were detected using a multibeam echo-sounder and CTD rosette measurements. These acoustic plumes are detectable in the water
40 column from the seafloor up to around 500 mbss and are distributed over 23 active emission sites to this day (Fig. 1) while the specific origin of these magmatic fluid emissions has yet to be determined (Mastin *et al.*, 2023).

The ocean circulation around the Mayotte island, and more generally in the Mozambique Channel, is part of the Agulhas Current. This current is one of the strongest and most regular known, as well as the strongest in the Southern Hemisphere with a western land boundary.

45 This highly complex circulation consists of a southward flow coupled with mesoscale eddies (diameter $\geq 300 \text{ km}$) that can affect the entire water column (de Ruijter *et al.*, 2002; Halo *et al.*, 2014). The general circulation in the area is even more complex due to the significant influence of the islands on the local hydrodynamic context.

There is also considerable variability in hydrographic parameters in the first 1,500 m of the water column. The temporal variability of these phenomena ranges from short-term (a few hours to a few days) to annual variations, due in particular to the
50 passage of anticyclonic eddies to the south. The signature of these eddies can be seen in hydrographic characteristics such as temperature and salinity. Strong deep currents ($\approx 0.4 - 0.5 \text{ m/s}$) are also present in the area, locally highly variable with strong interactions with the bathymetry.

Relatively little reference data is available for the area and it remains poorly understood. Tide gauges have been installed on the coasts of the main islands, and internal tidal waves have been observed during MAYOBS campaigns.

55 In order to monitor the dissolved gas dynamics related to volcanic events in the Horseshoe area and as a complement to regular oceanographic cruises, SeaExplorer glider deployments from ALSEAMAR (<https://www.alseamar-alcen.com/>) equipped with biogeochemical sensors are carried out since September 17, 2022 with funding from REVOSIMA. The SeaExplorer glider is a member of the family of autonomous underwater drones that can provide continuous collection of high-resolution underwater data between the surface and its maximum depth rating (1,250 m) over very wide spatial (several thousand kilometers) and
60 temporal (up to two months) coverage. Supervised by an Iridium satellite link, the vehicle enables near-real-time observation and monitoring of the oceans from a control center on land. The Global Ocean Observing System (GOOS), led by the Intergovernmental Oceanographic Commission (IOC) of UNESCO, and co-sponsored by the World Meteorological Organization (WMO), the United Nations Environment Programme (UNEP) and the International Science Council (ISC), has been coordinating national ocean observing efforts for more than 20 years. In this international effort, the role of autonomous glider
65 observations has always been seen as a means to compensate for the limitations of other observing means (Stommel, 1989).



The contribution of gliders began in earnest in the 2010s, when the technology was mature enough to contribute to global observations (Testor et al., 2010).

2 Data and Methods

2.1 Mission overview

70 The glider has been deployed at sea near to the eastern coast of Petite-Terre since September 17, 2021 (12 km southwest of the Horseshoe area 12°53.5', 45°19' E). It is operated for 14 days periods on average before being recovered at sea to recover the full dataset. The glider is then immobilized on land for one night to recharge the battery before being redeployed the next day. In the course of more than two and a half years of deployment, six gliders have been used for 72 deployments (see Appendix A table A1).

75 These gliders are equipped with a CTD (conductivity, temperature, depth), either a GPCTD from SeaBird or LEGATO CTD from RBR. Dissolved oxygen sensors are also deployed, an SBE43F from SeaBird coupled with the GPCTD and an AROD-FT from JFE coupled with the LEGATO. The scientific payload also includes an ADCP 1MHz from Nortek (Signature1000 specs with casing modified for glider integration AD2CP), a METS (dissolved methane sensor) from Franatech and a MINICO2 (dissolved CO_2 sensor) from Pro-Oceanus (see Appendix A table A1).

80 To carry out the mission, a specific and unusual sampling strategy was implemented. Until August 2023, the glider was limited to its maximum depth of 1000 mbss, so in order to stay as close as possible to the seafloor where magmatic fluid emissions occur, the glider's navigation consisted in a downward phase where the glider reached a depth of 1,000 mbss, followed by about ten ascent/descent phases (i.e. yo) between 900 and 1,000 mbss, followed by a final phase of ascent to the surface. Transects carried out in the Horseshoe area last on average 8 to 9 hours, covering a distance of around 6 km. This radial navigation
85 strategy enables objective sampling of the zone of interest, covering all its quadrants equally, with maximum sampling effort at its center, decreasing progressively with distance (Fig. 2).

For the first time, two glider prototypes with a maximum immersion of 1,250 mbss have also been deployed in the area since August 2023. A slightly different navigation method was chosen, opting for spirals instead of straight transects. The radius of these spirals is 1.5 km, in order to cover the entire study area as closely as possible over the duration of a deployment.

90 Initially, a wide mapping of the area has been chosen until August 2023 to detect seeps and get an idea of the physico-chemical properties over a large area. With this new navigation method, sampling is then focused on better characterization of the seeps (Fig. 2).

These spirals also consist of a downward phase to a depth of 1,250 mbss, followed by several yos between 800 and 1,250 mbss, and finally an ascent to the surface. These types of dives last an average of 10 hours. This sampling method was chosen to
95 ensure the good quality of data from dissolved gas sensors by flushing the sensors (see section 2.2.2) and to focus the navigation on known active sites and their immediate surroundings.



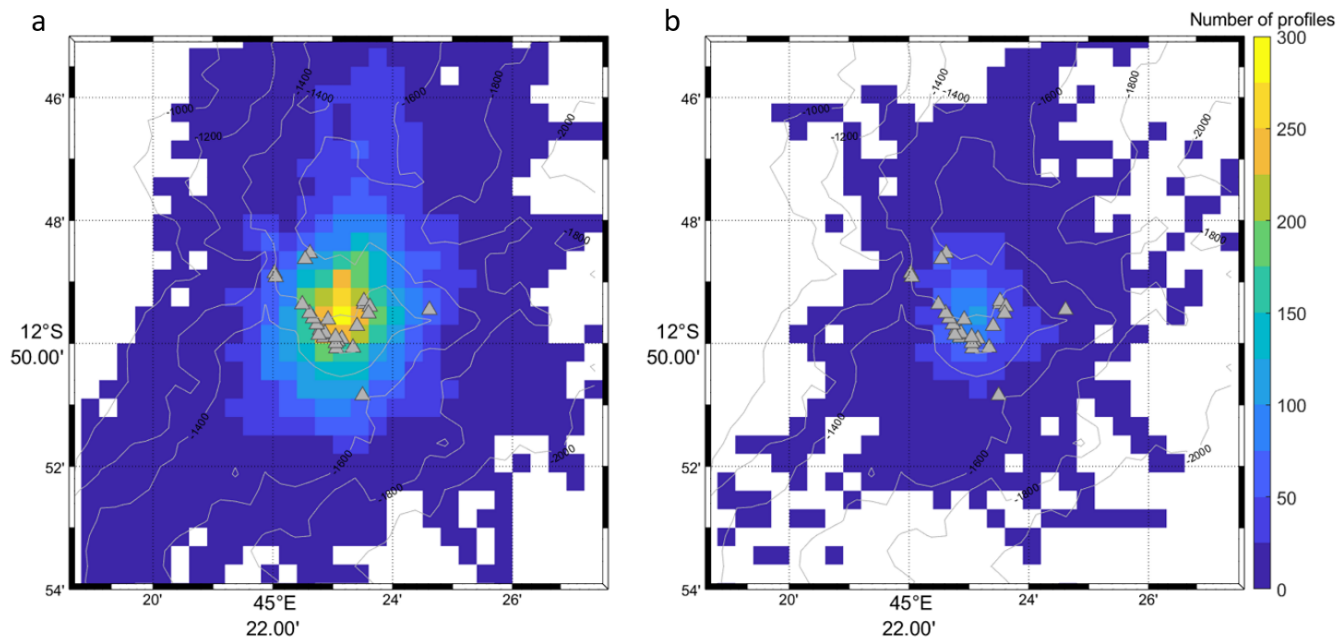


Figure 2. Map illustrating the sampling effort based on the number of profiles acquired below 1000 mbss max depth rating SeaExplorer in rectangles of 1 km^2 (a) and map illustrating the sampling effort based on the number of profiles acquired by the 1250 mbss max depth rating SeaExplorer in rectangles of 0.5 km^2 (b). The triangles are the active fluid emission sites identified with the multibeam echosounder during the REVOSIMA MAYOBS cruises (DOI 10.12770/070818f6-6520-49e4-bafd-9d4d0609bf7d) and validated by in situ visual observations with the ROV VICTOR during the GEOFLAMME cruise (DOI 10.17600/18001297). Isobaths are processed from GEBCO gridded bathymetry data (DOI 10.5285/1c44ce99-0a0d-5f4f-e063-7086abc0ea0f).

2.2 Data processing

2.2.1 CTD and DO data

For the sensor pair GPCTD and SBE43F processing, the salinity (SAL) is derived from raw conductivity measurements and the density is approximated with the 48-term function of temperature (TEMP), salinity and pressure (PRES). Computations were performed according to international standards and using TEOS-10 GOOS standards (http://www.teos-10.org/pubs/IOC-XXV-3_e.pdf).

Data processing is carried out in accordance with OceanGlider SOPs (Lopez-Garcia *et al.*, 2022, <https://github.com/OceanGlidersCommunity>). Moreover, the thermal lag effect was described and addressed using the methodology described in Garau *et al.*, 2011.

Computation of dissolved oxygen data in physical units was performed following Owens and Millard, 1985 algorithm.

For the sensor pair LEGATO CTD and AROD-FT, the data are processed internally by the sensors. Dissolved oxygen data are directly available in $\mu\text{mol}/\text{kg}$ while SAL data is also computed from the conductivity cell within the sensor.



O_2 time-series acquired with the different sensors used underwent large discontinuities, which were ubiquitously related to instrumental deficiencies. To face with this issue, the time-series was split into discrete segments according to the different regimes, all based on Ocean Glider SOP (Lopez-Garcia *et al.*, 2022). The assembled proposed adjustments (gain and/or constant offset over depth) were applied to make the entire glider time-series continuous. Gain values applied for each discontinuity can be found in Appendix B table B1. Sensors unit, range, precision and resolution can be found in Appendix C table C1.

2.2.2 Dissolved gases data

The response time of membrane-based sensors is a major constraint for profiling platforms (Fiedler *et al.*, 2013). Although the glider is a rather slow profiling device, the MINICO2 response time cause an appreciable hysteresis in vertical CO_2 profiles. A time-lag correction algorithm (Miloshevich *et al.*, 2004) has been applied on carefully smoothed vertical profiles of CO_2 (to minimize noise amplification caused by the processing algorithm), using the following model, sequentially:

$$CO_{2,corr}(t) = \frac{CO_{2,raw}(t) - CO_{2,raw}(t-1)e^{-\frac{\Delta t}{\tau}}}{1 - e^{-\frac{\Delta t}{\tau}}} \quad (1)$$

Where $CO_{2,raw}(t)$ is the measured value at the time t , $CO_{2,raw}(t-1)$ is the measured value at the previous time stamp, Δt is the time between two measurements, $CO_{2,corr}(t)$ is the time-lag corrected (TLC) measurement at t and τ is the response time. Previous studies have shown pronounced changes in τ that linearly depends on water TEMP (Fietzek *et al.*, 2014): the warmer the water, the faster the response time. In the absence of published values for the MINICO2 sensor, the linear relationship was determined empirically minimizing the difference in CO_2 between upcast and downcast profiles of a dive. Finally, raw CO_2 data recorded in ppm were converted in $\mu mol/l$ from manufacturer calculation sheet and using in-situ temperature and salinity values measured by the CTD.

The measurement of CH_4 might be impacted by various external factors such as temperature, in-situ CH_4 or the moving speed of the glider. Main consequences are an artificially increasing CH_4 with decreasing temperature, an hysteresis between the uplift and the downlift phases of a profile and thermal and temporal lags (Meurer *et al.*, 2021, Russell-Cargill *et al.*, 2018).

In the present study, these issues were first addressed by adapting the sampling strategy. Indeed, the glider was programmed to dive in deep multiple yos to limit the impact of varying environmental conditions. This way, it is expected that temporal changes in CH_4 (e.g. induced by natural seepage) would be more easily detectable compared to a situation where the glider would cross regularly strong temperature gradients. Comparison of CH_4 profiles between uplift and downlift phases enabled the computation of a lag in the sensor response time (τ) of about 6 minutes. Adjusted CH_4 ($CH_{4,corr}$) were thus calculated following the Meurer *et al.*, 2021 algorithm:

$$CH_{4,corr}(t) = CH_4(t + \tau) \quad (2)$$

where t is the time, while τ varies according to the sensor used (Appendix A table A1). Sensors unit, range, precision and resolution can be found in Appendix C table C1.



2.2.3 ADCP data

140 For the purpose of this project, the ADCP was programmed to obtain water-current profiles with a high-resolution. Values of main tunable parameters can be found in Table 1. The method used to retrieve ocean currents is the “shear method” (Visbeck,

Table 1. ADCP configuration and processing



Parameter	Description	Values
Position	Sensor mounting	Downward looking
NPING	Number of ping averaged	4
CS	Cell size	1 m
CN	Number of cells	30
SR	Sampling rate	10s

2002).

It is worth noting that glider ADCP measurements must undergo several quality control steps before profiles of ocean velocity can be properly estimated. It is a critical issue and this must be done with great caution. Pasqueron de Fommervault *et al.*,
145 2018 developed a number of tests specifically adapted for the SeaExplorer glider. The quality of the dataset was assessed at the end of each mission by comparing the depth-integrated water-current between two consecutive surfacings to the mean current deduced from the hydrodynamical model of the glider.

The processing of water-current data requires to reconstruct vertical profiles by cutting the time-series on the basis of dives. In case of multi-yos, which not optimal to retrieve best quality water-current measurements, all yos between two consecutive
150 surfacings are merged to reconstruct a single average water-current profile. Since the tidal current oscillates over a period of about 12 hours, its oscillations are therefore almost always averaged over the duration of a transect.

While ADCPs are primarily used to measure the velocity of the particles, they can also provide information about the backscatter index (BI) that in turn is a proxy of the density of backscatterers in the water-column. This information is measured in the form of the intensity of the received reflections, also referred to as the backscattering strength or signal amplitude. The method
155 to retrieve BI from raw ADCP measurements employs a formula based on the sonar equation for sound scattering from small particles (Deines, 1999; Van Haren and Gostiaux, 2010; Mullison, 2017; Gentil *et al.*, 2020):

$$BI = EI + Tl_g + Tl_w \quad (3)$$

EI is the echo intensity estimated from ADCP signal amplitude from all beams using the Mullison (2017) equation. Tl_g is the beam spherical spreading, which is simply a geometric term due to the cone shape of the acoustic beams. Tl_w is the
160 transmission loss by the sound absorption in seawater calculated according to Francois and Garrison (1982) and taking into account absorption by boric acid and magnesium sulfate.



2.3 Quality control process

An objective and automatic quality control (QC) procedure was applied on the basis of UNESCO oceanographic best practices (<https://repository.oceanbestpractices.org/handle/11329/413>). Quality flags (QF) is composed of four quality values (Table 2). The procedure allows to flag outliers but may be deficient in identifying some erroneous data. Tests presented hereafter relate

Table 2. Quality flag scheme

Quality flag value	Quality flag name	Definition
1	Good	Passed quality control
2	Not evaluated	QC test not performed
3	Suspect	Failed subjective QC test
4	Bad	Failed objective QC test

165

to the other variables and are based on published methods (Pouliquen 2011, Schmechtig *et al.*, 2016) and recommended by the scientific community within international programs, such as EGO quality control manual for CTD and BGC (BioGeoChemical) data (<https://archimer.ifremer.fr/doc/00403/51485/92689.pdf>, 2022).

A gross filter is applied on observed data using a global range test first (Table 3) with min and max values taken from EGO quality control manual.

170

Values that fail this test are flagged with a QF = 4. To our knowledge there are not yet international recommendation for CH_4 and CO_2 , thus values were chosen based on in situ measurements from MAYOBS cruises.

For all parameters, data acquired when the CTD pressure is negative (i.e. in-air measurement) were flagged bad (QF = 4).

Table 3. Global range test used for QC

Parameter	Min value	Max value
Temperature [°C]	-2.5	40
Salinity [PSU]	2	41
Dissolved oxygen [$\mu\text{mol}/\text{kg}$]	-5	600
Dissolved CH_4 [nmol/l]	0	2000
CO_2 [$\mu\text{mol}/\text{l}$]	5	100

Furthermore, a large difference between sequential measurements, where one measurement greatly differs from adjacent ones, were also flagged bad if failing the following algorithm (only used to identify spikes in temperature, salinity and O_2 profiles, EGO quality control manual, 2022):

175

$$T_{\text{test}} = \left| \frac{V_2 - (V_3 + V_1)}{2} \right| - \left| \frac{V_3 - V_1}{2} \right| \quad (4)$$



where V_2 is the measurement being tested as a spike, and V_1 and V_3 are the values preceding and ensuing. The V_2 value is
180 flagged when the test value exceeds:

TEMP : 6.0°C for PRES < 500 db or 2.0°C for PRES ≥ 500 db

SAL : 0.9 for PRES < 500 db or 0.3 for PRES ≥ 500 db

O_2 : $50 \mu\text{mol}/\text{kg}$ for PRES < 500 db or $25 \mu\text{mol}/\text{kg}$ for PRES ≥ 500 db

To our knowledge there are no international recommendations for CH_4 and CO_2 yet. Thus, no spike test was applied on these
185 variables.

Finally, subjective visual inspection was performed for each variable to identify outliers that were not flagged by the automatic
and objective procedure. These measurements were associated with a QF = 3.

Membrane-based sensors (CO_2 and CH_4) are also deficient at high glider's speed (lag cannot be compensated correctly).
Thus, CO_2 and CH_4 data acquired at glider's speed exceeding 0.25 m/s were flagged and excluded. This typically occurs
190 when the glider ascend in alarm state which is rather rare.

All data provided has been quality controlled. Therefore, QF = 2 is not used in this dataset.

Following these various objective and subjective tests, the remaining data volume of each data is provided in the Appendix D
table D1.

Every 6 months, a reassessment of the processing chain (algorithm, QC) and delayed mode adjustments (drift, offset) is pro-
195 posed.

3 Results and discussion

3.1 Hydrological dataset

Hydrological data presented are adjusted and associated with a QF = 1.

Time-series of temperature, salinity and density are presented in Fig. 3, averaged vertical profiles are presented in Fig. 4 and
200 temperature-salinity diagram exhibiting the different water masses is shown in Fig. 5.

As for temperature, vertical profiles exhibit a relatively warm upper layer ($\sim 0\text{-}100$ mbss, $26\text{-}30^\circ\text{C}$). The seasonal thermocline
(steep thermal gradient of $\sim 0.1^\circ\text{C}/\text{m}$) is observed between $\sim 100\text{-}200$ mbss and the permanent thermocline is located at ~ 500
mbss and is mainly composed of South Indian Central Water (SICW, Miramontes *et al.*, 2019). Below 500 mbss, temperature
are in the range $5\text{-}10^\circ\text{C}$, with a minimum reached below 1000 mbss. In this layer, both Red Sea Water (RSW), that enters
205 into the Mozambique Channel from the north, and Antarctic Intermediate Water (AAIW), that enters from the south are found
(Miramontes *et al.*, 2019).

The vertical distribution of the salinity is more complex. Overall, the upper layer is characterized by values ranging from \sim
 34.7 and 35.5 PSU. A subsurface salinity maximum is observed at $\sim 200\text{-}300$ mbss with salinity values reaching up to 35.5
PSU. At around 600 mbss, a local salinity minimum ($34.6\text{-}34.8$ PSU) is observed but followed by a slight increase to reach
210 ~ 34.85 below 1000 mbss. Deeper in the water-column (i.e., below ~ 100 mbss), the variability in hydrological properties is
lower. However, disruptions in the vertical distribution of temperature and salinity is clearly viewable and can be attributed

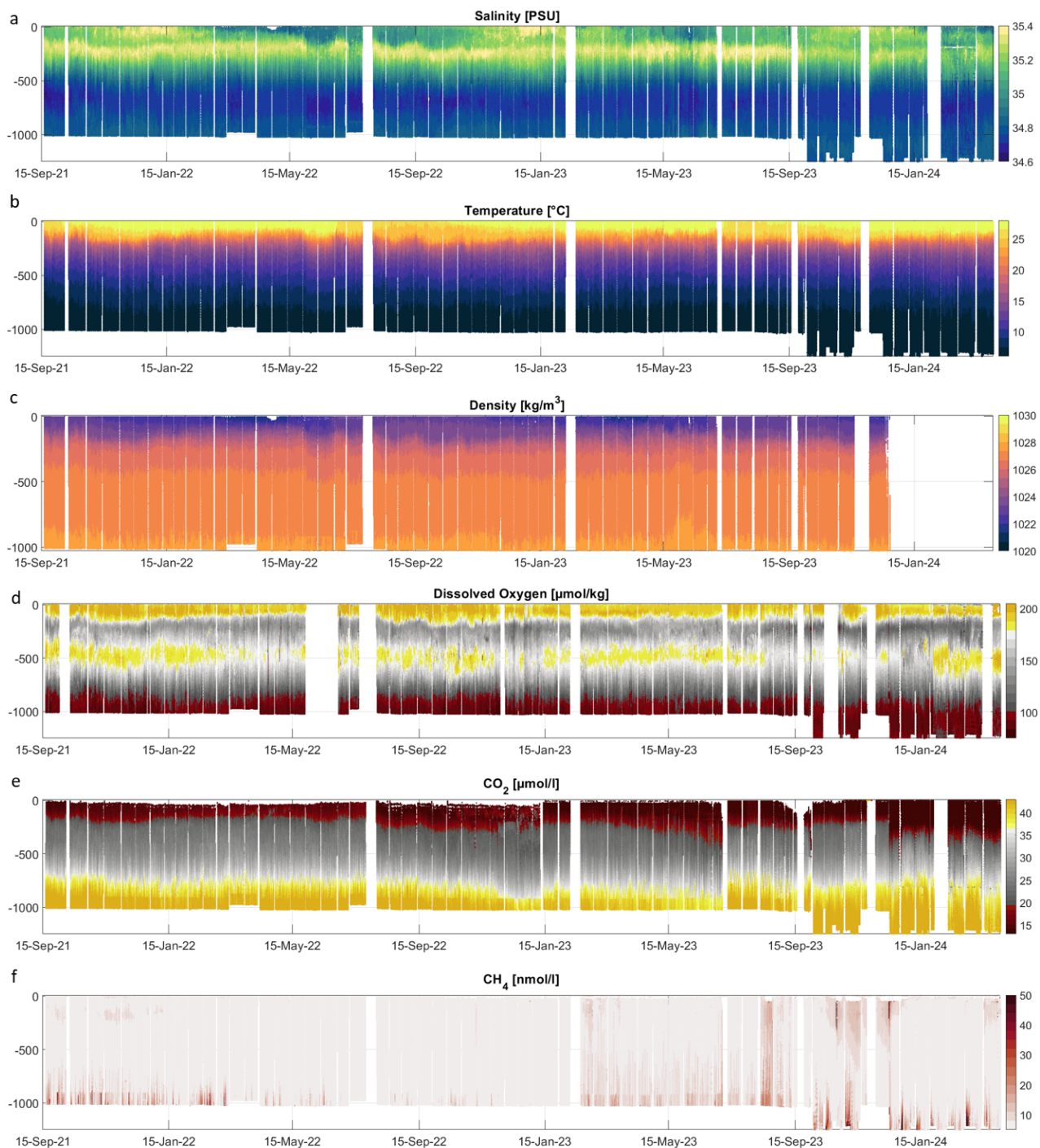


Figure 3. Salinity (a), temperature (b), density (c), dissolved oxygen (d), CO_2 (e) and CH_4 (f) Hovmöller diagram in function of depth (Y-axis) and time (X-axis)



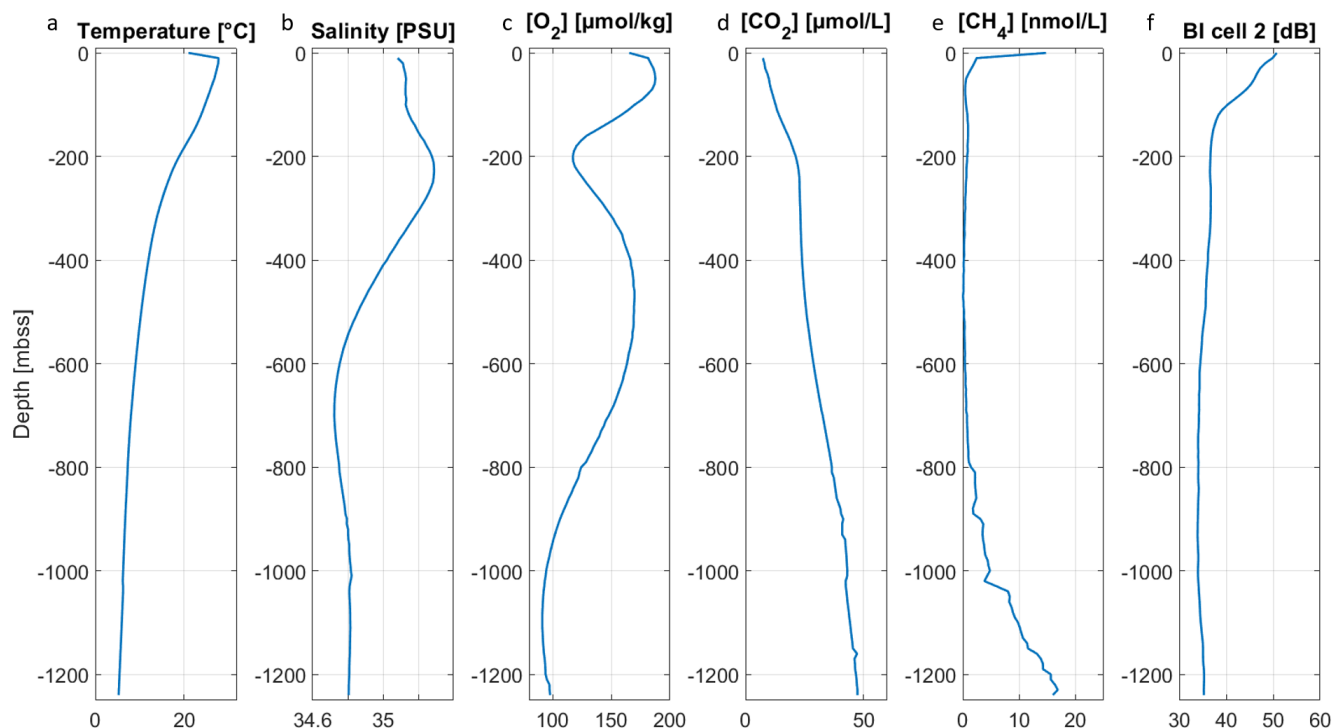


Figure 4. Averaged vertical profiles of temperature (a), salinity (b), O_2 (c), CO_2 (d), CH_4 (e) and Backscatter Index calculated from the cell 2 of the ADCP (f) over 10 meter bins for the whole dataset.

to the general circulation of the area or the mesoscale variability. Below 1,000 mbss the variations are $\sim 1^\circ\text{C}$ and ~ 0.1 for temperature and salinity respectively (Fig. 6).

Most of the temporal variability is observed in the surface layer, above the 1024 kg m^{-3} isopycnal. These changes are particularly obvious in the temperature-salinity diagram (Fig. 5), but are puzzling. They can indicate the succession of two distinct water-masses. Indeed, low salinity are typical of the Tropical Surface Water and contrasts with the higher salinity Subtropical Surface Waters (Di Marco *et al.*, 2002). Surface temperature exceeding 29°C (which are regularly observed from December to April, Fig. 4 and 7) can also be the signature of the influence on the South Equatorial Current that contains Pacific waters (Di Marco *et al.*, 2002) or associated to the transient presence of mesoscale eddies. Finally, and according to Wyrтки (1971), seasonal processes (and episodically tropical storms) may also account for the observed variability. Highest sea-surface temperatures and low salinity are generally observed during austral summer while in winter, colder and saltier waters dominate. This seasonal variability is observed in this part of the water column (Fig. 7), with warm ($\sim 27 - 28^\circ\text{C}$) and salty ($\sim 35.3 - 35.4$) surface waters from November 2021 to July 2022 and from October 2022 to July 2023 during warm and humid austral summer in Mayotte.

The analysis of the dataset also highlighted the importance of processes of smaller temporal scales. In particular, vertical fluctu-

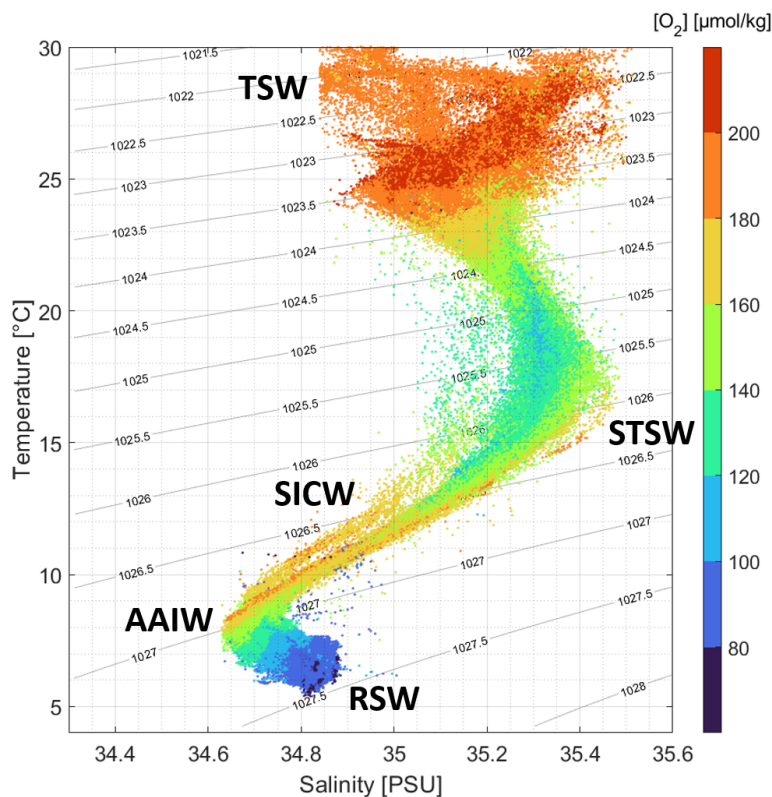


Figure 5. Temperature salinity diagram. The color indicates the O_2 concentration and the water masses associated are written. TSW stand for Tropical Surface Water, STSW for Subtropical Surface Waters, SICW for South Indian Central Water, AAIW for Antarctic Intermediate Water and RSW for Red Sea Water.

tuations of density levels (and temperature and salinity) of several dozen meters were observed at a ~ 12 h period (Fig. 7). Likely a result of internal tides, the adopted sampling strategy does not allow for their quantification and study (section 2.2.3).

3.2 Dissolved gas dataset

Similarly to the hydrological dataset, data presented are adjusted and associated with a $QF = 1$.

230 Measured O_2 , CO_2 and CH_4 concentrations by the glider are shown in Fig. 3. Typical vertical distributions are observed (Fig. 4) and can be explained by ubiquitous physical (e.g., dissolution, sea-air exchanges) and biological oceanic processes (photosynthesis and respiration).

High O_2 concentrations corresponding to oxygen saturation concentration are measured ($180\text{-}200 \mu\text{mol/kg}$, Fig. 3 and 4) at the surface layer (0 - 100 mbss) because of both dissolution from the atmosphere and O_2 production by phytoplankton. As
235 the distance to the surface increases O_2 generally declines, due to O_2 removal by consumption of deep-water organisms and by the decomposition of organic material by bacteria (Hedgpeth, 1957). In the glider dataset, minimum O_2 values (O_2 in the

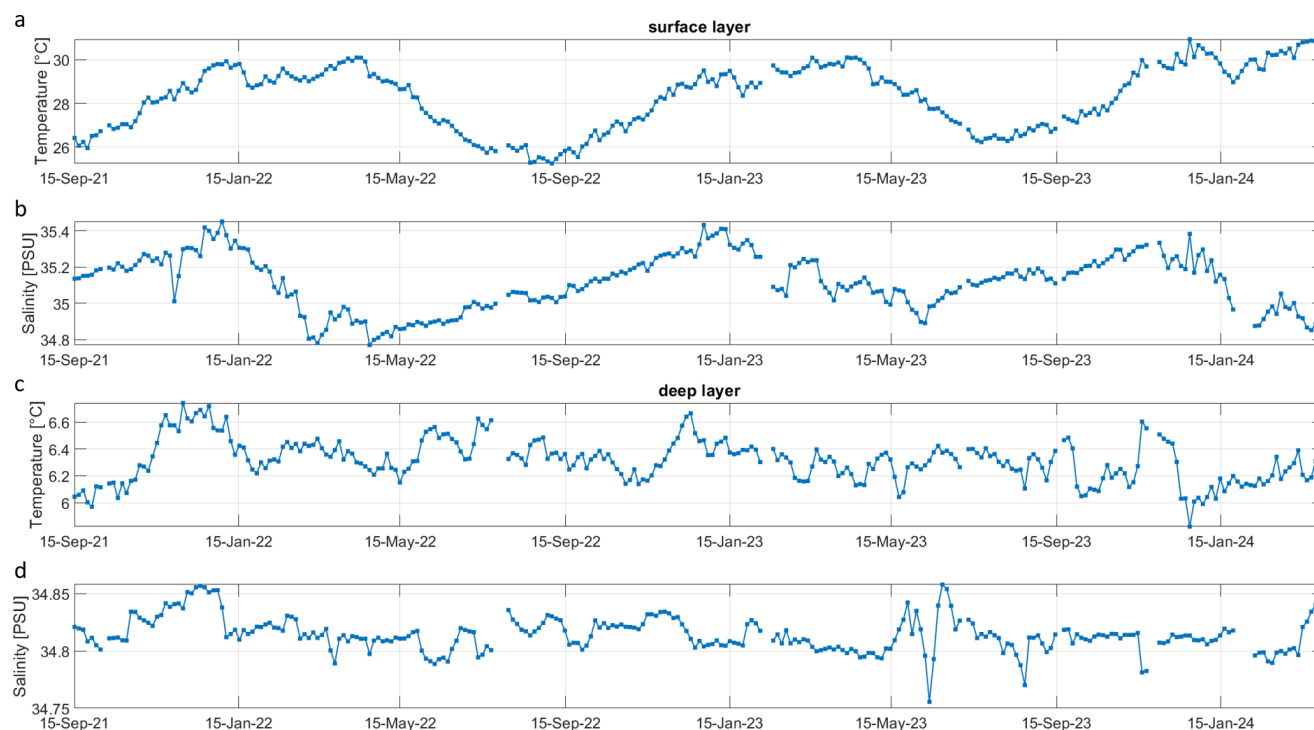


Figure 6. Surface layer (0 to 5 mbss) daily average temperature (a) and salinity (b) and deep layer (950 to 1,250 mbss) daily average temperature (c) and salinity (d).

range 70-100 $\mu\text{mol}/\text{kg}$) are observed below 1,000 mbss. In spite of this decrease, O_2 content rise to a subsurface maximum at ~ 400 -500 mbss with values reaching up to 200 $\mu\text{mol}/\text{kg}$. This high O_2 core ($> 180 \mu\text{mol}/\text{kg}$) is characteristic of the South Indian Central Water (Di Marco *et al.*, 2002).

240 Regarding the CO_2 vertical distribution (Fig. 4), it is essentially the reverse of O_2 , mainly because both gases are involved in the same biological processes in opposite ways. In the surface, photosynthesis consumes CO_2 and thus concentrations are low ($\sim 15 \mu\text{mol}/\text{l}$). In deeper waters, CO_2 concentration increases as respiration exceeds photosynthesis and decomposition of organic matter adds additional CO_2 to the water. In this dataset, minimum CO_2 concentrations are found in the surface layer (0 - 100 mbss) with concentrations measured between 15-20 $\mu\text{mol}/\text{l}$, and maximum CO_2 values are measured below 1,000 mbss
245 depth with concentrations generally higher than 40 $\mu\text{mol}/\text{l}$ and sporadically exceeding 50 $\mu\text{mol}/\text{l}$. Moreover, the signature of SICW with its oxygen maximum at ~ 400 -500 mbss (Di Marco *et al.*, 2002) is not matched by a CO_2 minimum at this depth. The vertical distribution of CH_4 differs significantly from the ones of O_2 and CO_2 (Fig. 3 and 4). Almost no CH_4 is detected in the layer 0-600 mbss (values are below 10 nmol/l). This is not surprising because the ocean is supposed to be depleted in CH_4 apart from specific areas (methanogenesis in marine sediment, natural seepage by volcano or hydrothermal vents, pollution,
250 Oremland *et al.*, 1978). Most of CH_4 increases occur in the 900-1,250 mbss layer where the sampling effort is maximum. In

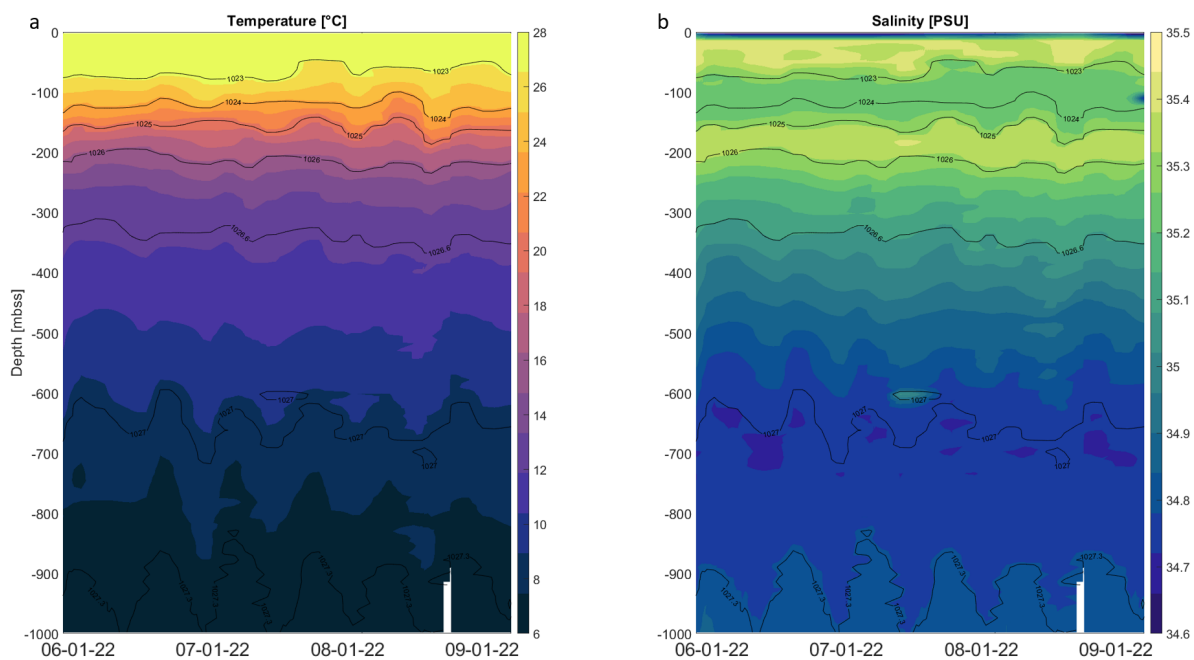


Figure 7. High-frequency (~ 12 h period) oscillations of temperature (a) and salinity (b) in function of depth (Y-axis) and time (X-axis). Isopycnes are also calculated and displayed. Data is interpolated with a triangulation-based cubic interpolation over a 12 m grid.

this layer, when CH_4 anomalies are detected (above the sensor detection limit), a gradient of increasing concentration with depth is observed. High values relative to the background are regularly observed with a maximum recorded on February 18, 2022, when CH_4 reached 120 nmol/l at a 1,000 mbss. Although observations above 900 mbss are scarce, several vertical profiles show also significant CH_4 concentrations up to 700 mbss.

255 There is also variability in dissolved gas concentrations, with periods (e.g., September 2022 to mid-October 2022 and mid-November 2022 to February 2023) of decreasing CH_4 or CO_2 concentrations not yet explained (Fig. 8).

The amount of data produced during continuous acquisition at high sample rates is substantial (~ 2.2 million measuring points per sensor corresponding to $\sim 22,000$ profiles), and semi-automatic methods are thus required to reduce this data set to relevant information. Here we focus on parameters that track magmatic fluid emissions (CO_2 and CH_4) and we define anomalies as
260 observations that deviate significantly from the majority of the data.

Identifying anomalies (that refer to fluid emissions) is challenging since it requires the de-coupling between natural variability (e.g. water-masses, seasonality) and changes induced by fluids emissions. In particular, CO_2 and CH_4 signals are characterised by slowly varying background values related to dissolved gases accumulation and flushing over a large area. The CH_4 baseline is low ($<10 \text{ nmol/l}$) and has a magnitude of variability of about 6 nmol/l . On the other hand, CO_2 baseline is more elevated
265 ($\sim 45 \text{ } \mu\text{mol/l}$ at a 1,250 mbss), because of the natural presence of CO_2 in seawater and CO_2 anomalies below 900 mbss, but fluctuations around the mean values do not exceed $\sim 3 \text{ } \mu\text{mol/l}$.



Results also show that both CO_2 and CH_4 baselines have similar temporal evolutions, supporting the hypothesis that this variability is likely to be real. For the purpose of anomaly detection, the baseline was thus subtracted to the raw data:

$$Gas, anomaly_{deep}(t) = Gas, measured_{deep}(t) - Gas, baseline_{deep}(t) \quad (5)$$

270 However, the cause of this low-frequency variability still remains to be clarified. At this time, it is not clear if baseline fluctuations are related to accumulation/dispersion processes or induced by changes in fluid emissions rate, both compatible with the chosen anomaly definition.

Of the 22000 profiles, 5 % were associated with significant CH_4 anomalies (greater than the sensor detection limit plus twice the standard deviation) and 2 % with significant CO_2 anomalies related to dissolved gas emissions (same definition as for the
275 CH_4).

Data show that CO_2 and O_2 have similar patterns. Such a co-variation is expected in the ocean and related to biotic processes. Examining this relation at depth > 700 mbss (i.e., below the STSW) indeed confirms a high CO_2 and O_2 correlation (linear correlation coefficient, $R^2 = 0.96$). Several single measuring points deviate from the linear relationship (Fig. 8). They are all found in the upper curve, i.e. at depth where CO_2 is high and O_2 low. Most of these points are also associated with high CH_4
280 concentrations, which strongly suggests that these CO_2 anomalies are related to a non-biotic CO_2 source.

3.3 Ocean current and acoustic backscatter dataset

ADCP-derived water currents show a large profile-to-profile variability that encompass, in all likelihood, spatial and temporal variability. Strongest currents are measured in the surface (0-100 mbss layer) but velocities remain elevated up to 1,250 mbss
285 (Fig. 9).

Overall, eastward velocities do not exhibit clear patterns. Values are oscillating with no preferential direction (Fig. 9). Conversely, northward velocities are characterized by a distinguishable temporal variability. From several weeks to several months, the current direction changes, with long periods of time when the direction of flow remains unchanged.

Backscatter data estimated from ADCP measurements and expressed as the backscatter index (BI) are represented on Fig. 4 as
290 an averaged profile. This averaged profile primarily depicts water-masses optical properties changes which are determined by phyto- and zoo-plankton abundance, mineral particles concentration (Mullison, 2017; Gentil *et al.*, 2020). Thus, and as it can be expected, BI shows maximum values in the surface layer (0-100 mbss), where most of the biological activity takes place. Deeper in the water-column, BI is generally lower, although sometime peaking at the level of the South Indian Central Water and in the ~ 900 -1,250 mbss layer when crossing dissolved gases plumes or moving around the seafloor.

295 Similarly, the BI variability in the surface mirrors changes in temperature and salinity to a certain extent and several glider transects showed a BI increase at depth, when the glider approaches the continental shelf. This variability is not fully understood and likely to be a multi factor cause resulting in a decoupling of the surface, subsurface and deep dynamics. Whatever the processes envisioned, in all likelihood, a direct contribution of magmatic fluid emissions can be discarded.

In the other hand, BI profiles are noisy and variable with depth and despite this large variability, the signature of bubble/droplets

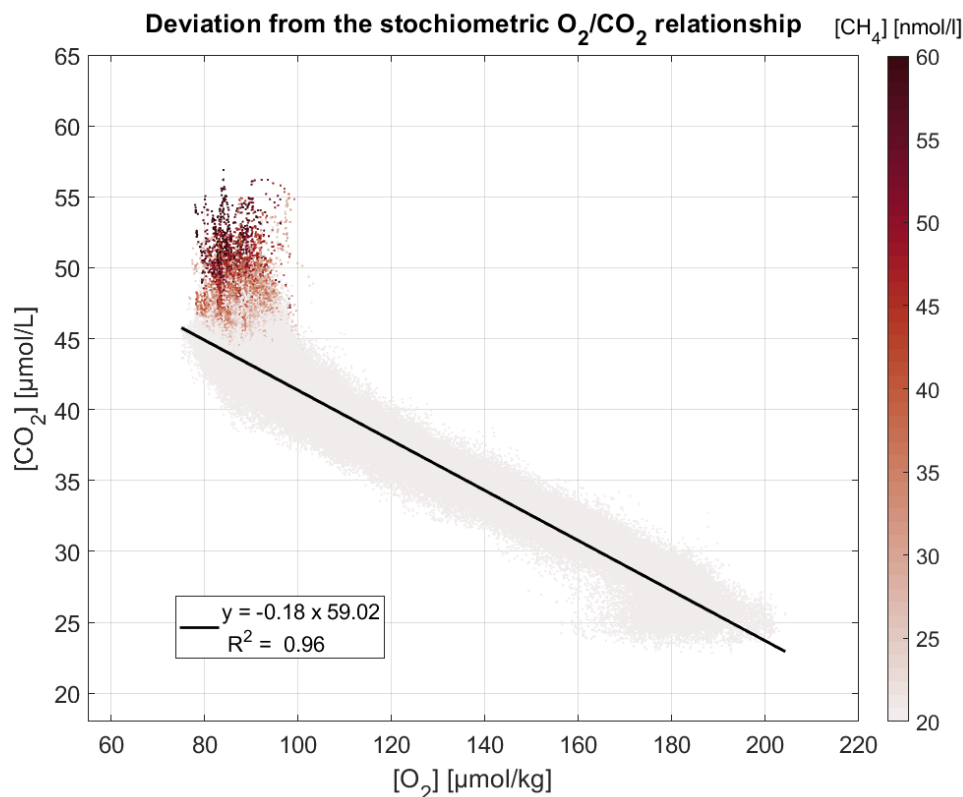


Figure 8. O_2/CO_2 relationship below 600 mbss, the colorbar indicates the CH_4 concentration. Data are taken from September 2021 to January 2023 and below 600 mbss.

300 appears to be unambiguous, associated with a large density of positive spikes of great amplitude and associated vertical velocity anomalies of about 15 cm/s , which is the ascent velocity of gas droplets in the ocean (Rehder et al., 2009; Leblond et al., 2014, Fig. 10). BI increases in the deep layer were considered to be related to acoustic plumes if several consecutive BI values exceed $\sim 50 \text{ dB}$ in at least 6 cells of the ADCP to discard the few possible misdetection at this depth. This was used as a criterion for BI anomaly detection but each transect was also visually inspected.

305 Of the 22,000 profiles, 457 ($\sim 2\%$) were associated with significant BI anomalies. The relative low occurrence of BI detections indicates that acoustic plumes are likely to be of limited spatial extension (\sim hundreds of meters) especially compared with dissolved and neutrally buoyant gas plumes.

Although associating BI detections directly to an active site is complex (uncertainty in glider positioning, tilt of droplets/bubbles plumes of several hundred meters because of deep and tidal currents), data show that most of known sites were indeed
310 identified by the glider. 95% of BI detections are found within a radius of 700 m from an active site and the remaining 5% always at a distance less than 1.6 km.

Repeated dissolved gases and BI anomalies in the 800-1250 mbss layer (Fig. 10) provide evidence that elevated CO_2 anomaly

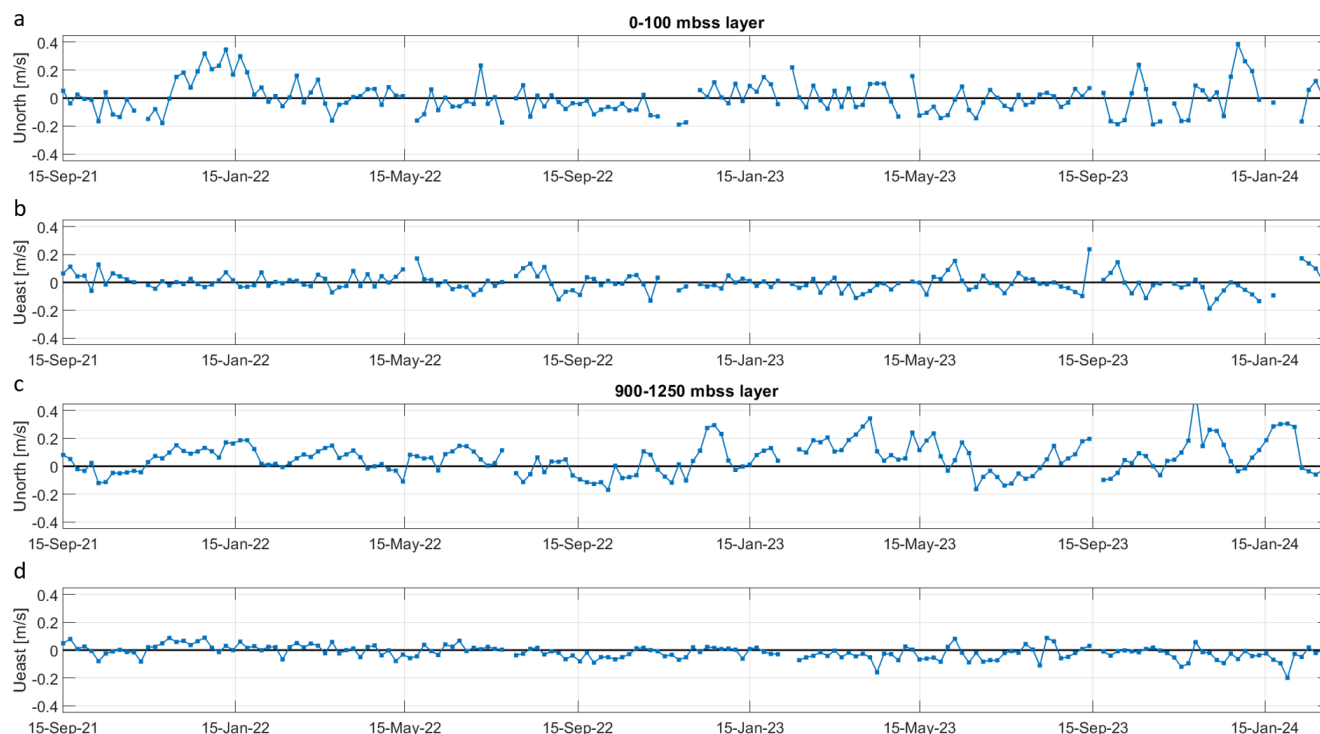


Figure 9. Time-series of northward (a) and eastward (b) velocities measured by the ADCP in the 0-100 mbss layer and time-series of northward (c) and eastward (d) velocities measured by the ADCP in the 900-1250 mbss layer. Data represented are daily mean values averaged in each layer.

lies in the 900-1250 mbss layer are related to magmatic fluids emissions.

BI detections outside of the 95th percentile are observed around the Horseshoe zone may arise from intermittent, small, 315 unidentified sites or false detections. Further analysis is needed to confirm the nature of these detections.

Temporal variations in dissolved gas concentrations (CH_4 and CO_2) and BI anomalies are presumably caused by a complex array of factors, including spatial variability related to the glider pathway. However, on the basis of our current knowledge, we assume that a large part of the observed changes can indeed be related to the variability of seafloor fluid emissions in the Horseshoe area as well as the orientation and direction of the current at depth.

320 Over the 30 months of deployments, values of CH_4 and CO_2 show some interesting patterns, with a large profile-to-profile variability observed in dissolved gas deep anomalies. High anomaly values exceeding the detection limit of the sensor plus two times the standard deviation (20 nmol/l for the CH_4 and $7 \text{ } \mu\text{mol/l}$ for the CO_2 anomalies) are observed throughout the time-serie. In the 900-1000 mbss layer (more than 90% of the dataset), the maximum CH_4 anomaly value is reached on February 21, 2022 (116.9 nmol/l) and the maximum CO_2 anomaly value on September 04, 2022 ($29.2 \text{ } \mu\text{mol/l}$).

325 Although a direct correlation between currents and gas anomalies is speculative, our data suggests a potential impact of

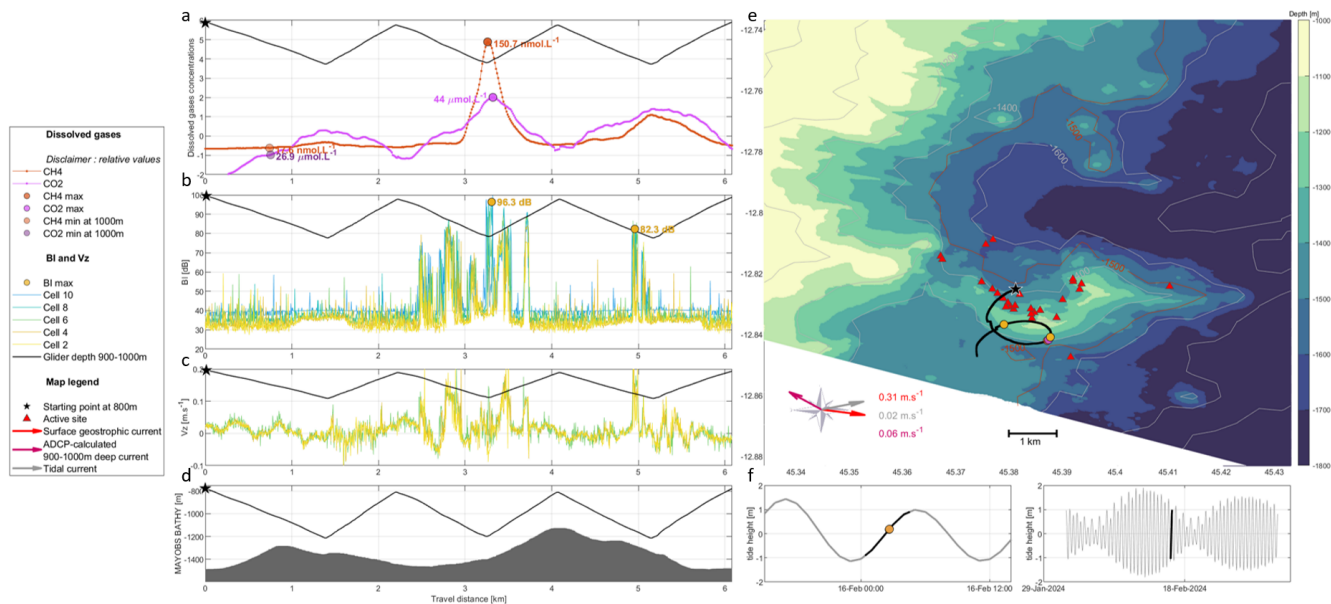


Figure 10. Example of 800-1250 spiral realised above know active sites. CO_2 and CH_4 concentrations are represented centered and reduced (to get a common representation of the two dissolved gases despite the different baselines and anomalies) as a function of the transect progress (a). The figure shows BI data (b), followed by vertical velocity calculated from the ADCP data (c) data and finally bathymetry along this transect (d). On the right are shown a map of the Horseshoe area with the glider position under water and the different current calculated during this transect (e) and the tide height modelised with MIKE21 model (f). Surface geostrophic current is estimated from sea level anomalies (SLA) data computed with respect to a twenty-year [1993, 2012] mean (<https://doi.org/10.48670/moi-00149>) and tidal current is modelised with MIKE21 model.

mesoscale structures on gas concentrations in the 900-1,250 mbss layer. The underlying processes are still poorly understood from the sole analysis of the glider dataset, but several processes would be worth to be investigated (trapping, dispersion, diffusion, upwelling, etc.). Furthermore, additional bottom current data could potentially greatly assist this analysis. In order to assess the spatial distribution, anomalies are plotted on maps (Fig. 11). This provides a comprehensive view of the area impacted by fluid emissions, over the 30 months duration of deployments. On Fig. 11, data are binned in 7 discrete concentrations intervals and superimposed from weakest to strongest values with circles of decreasing size. Only data that exceed criteria of detection are colored, and the maxima of the colorbar are equal to the 99th percentile. Highest gas anomalies were all observed in the center and in the immediate vicinity of the Horseshoe edifice and the magnitude of the anomalies progressively decrease as the glider moves away from the center. The radius of gas anomalies detection is around 10 km, and the total area impacted by fluid emissions spread over about 300 km^2 . These maps, that gather all data since September 17, 2021, also show that the distributions of gases anomalies are not isotropic. In particular, relatively high concentration relative to the far field are observed northward which can highlight a preferred export direction for these quantities of dissolved gas.

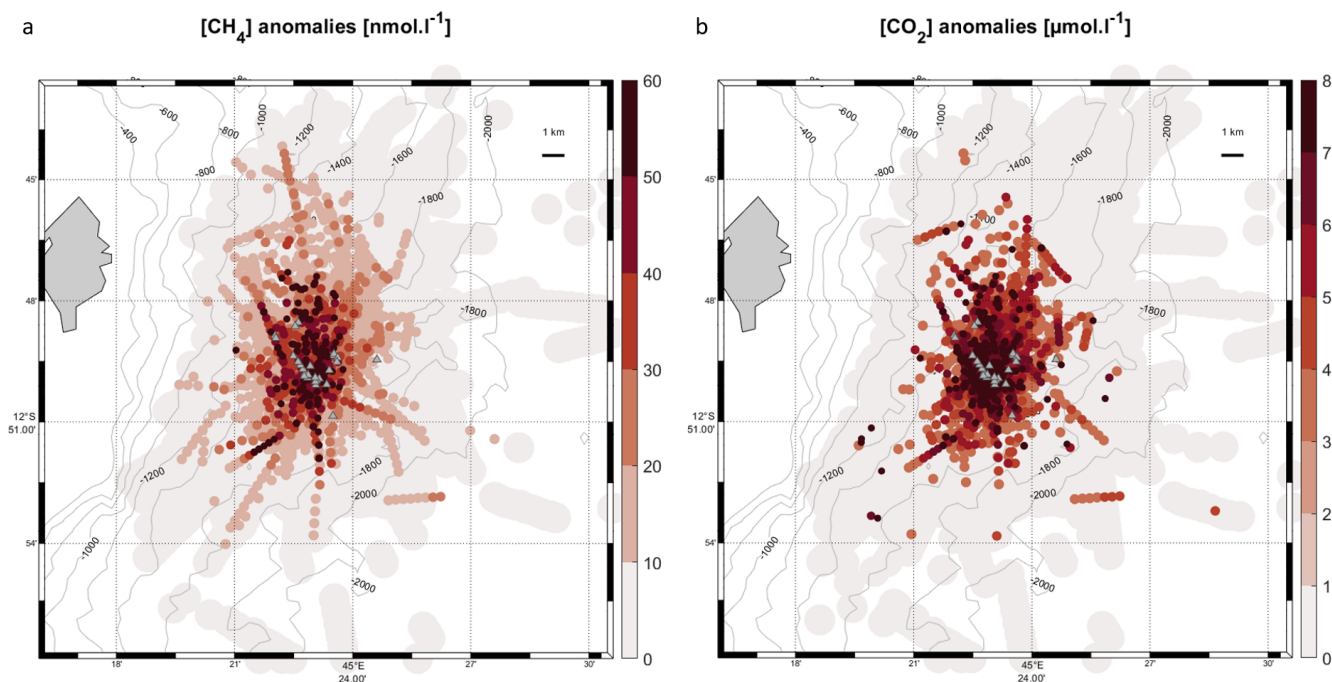


Figure 11. Map of CH_4 (a) and CO_2 (b) anomalies above the detection limit of these sensors recorded during the whole glider survey. The triangles are the active fluid emission sites identified with the multibeam echosounder during the REVOSIMA MAYOBS cruises (DOI 10.12770/070818f6-6520-49e4-bafd-9d4d0609bf7d) and validated by in situ visual observations with the ROV VICTOR during the GE-OFLAMME cruise (DOI 10.17600/18001297).

4 Conclusions

The overall quality of the produced dataset is remarkable and acquired without any interruption other than deployment/recovery period of the glider and fast repairs. CTD, dissolved gases (O_2 , CH_4 and CO_2) and ADCP data are available through this 30 months dataset in an area lacking reference data.

This is one of the few glider missions that has sampled CH_4 and CO_2 data, and it is also the longest glider time series of these variables that we are aware of. It also opens the possibility for new projects and research with the ability to identify these variables (GEORGE project, Hauri *et al.*, 2024).

The vertical distribution of hydrological, dissolved gas and BI data highlighted anomalies due to magmatic fluids in the Horseshoe area, while ADCP-calculated current depicted an active area subject to strong currents both at the surface and at depth. The data analysis is still ongoing but the glider platform showed its full potential to monitor, track and characterise fluid emissions off Mayotte island, making of this tool and ideal real time early warning system. In particular, the continuous monitoring at a high spatio-temporal scale of the 0-1250 mbss layer appears to be relevant to complement traditional oceanographic cruises (high-quality data but with a limited resolution) and to ensure an operational observing system.



The robustness of the platform (SeaExplorer glider) has also been demonstrated thanks to this dataset, with 901 days at sea over 929 days (97 % of its time spent at sea).

The quasi-permanence of elevated gas concentrations (CO_2 and CH_4) in the Horseshoe area support that fluid emissions are likely to have been continuous over the 30 months of the mission and detectable above 1250 mbss depth.

355 Regular detections of acoustic plumes above all identified active sites have provided direct evidence of active seepage during the survey and the presence of bubble/droplets above 1,250m-depth.

Many questions still remain in our understanding of the underlying processes. We can for example mention the spatial decoupling between acoustic and dissolved gas plume or the contribution of physical factors in modulating the extension, direction and intensity of the plumes (water-currents, internal tides).

360 To face with these scientific challenges, the synergy between the glider with other observations and measurement tools (CTD cast, ROV, moorings), numerical models and satellite products is promising. Several attempts in this direction have been initiated.

Reference data acquired during MAYOBS cruises allowed for a cross-calibration exercise of the dissolved gases sensors. An exercise has been carried out during the MAYOBS25 cruise in September 2023 by harnessing two gliders on the CTD cast in
365 order to compare dissolved gases from glider sensors and Niskin samples. The aim of these calibrations is to quantitatively calibrate dissolved gas sensors in order to calculate the fluxes of fluids emitted at the seabed.

Data availability. Raw and processed data are available from the SEANOE data center : <https://doi.org/10.17882/99960> (Heumann *et al.*, 2024).



370 Appendix A

Table A1. Glider missions performed

Deployment	Recovery	Glider	Mission ID	AD2CP	MINICO2	GPCTD	LEGATO	SBE43F	AROD	METS
17/09/2021	07/10/2021	SEA042	001	100584	39-636-18	0114		2610		1635
11/10/2021	27/10/2021	SEA042	002	100584	39-636-18	0114		2610		1635
29/10/2021	12/11/2021	SEA042	003	100584	39-636-18	0114		2610		1635
13/11/2021	29/11/2021	SEA042	004	100584	39-636-18	0114		2610		1635
30/11/2021	13/12/2021	SEA042	005	100584	39-636-18	0114		2610		1635
14/12/2021	27/12/2021	SEA042	006	100584	39-636-18	0114		2610		1635
28/12/2021	10/01/2022	SEA042	007	100584	39-636-18	0114		2610		1635
11/01/2021	21/01/2022	SEA042	008	100584	39-636-18	0114		2610		1635
22/01/2021	02/02/2022	SEA042	009	100584	39-636-18	0114		2610		1635
03/02/2022	16/02/2022	SEA042	010	100584	39-636-18	0114		2610		1635
17/02/2022	01/03/2022	SEA042	011	100584	39-636-18	0114		2610		1635
03/03/2022	14/03/2022	SEA042	012	100584	39-636-18	0408		3343		1635
15/03/2022	29/03/2022	SEA027	013	102759	39-636-18	0408		3343		1635
30/03/2022	10/04/2022	SEA027	014	102759	39-636-18	0408		3343		1635
13/04/2022	27/04/2022	SEA027	015	102759	39-636-18	0408		3343		1635
28/04/2022	12/05/2022	SEA027	016	102759	39-636-18	0408		3343		1635
13/05/2022	27/05/2022	SEA027	017	102759	39-636-18	0408		3343		1635
28/05/2022	11/06/2022	SEA027	018	102759	39-636-18	0408		3343		1635
12/06/2022	27/06/2022	SEA027	019	102759	39-636-18	0408		3343		1635
28/06/2022	08/07/2022	SEA027	020	102759	39-636-18	0408		3343		1635
10/07/2022	25/07/2022	SEA027	021	102759	39-636-18	0408		3343		1635
04/08/2022	16/08/2022	SEA017	022	102759	39-636-18	0408		3343		1635
17/08/2022	28/08/2022	SEA017	023	102759	39-636-18	0408		3343		1635
29/08/2022	12/09/2022	SEA017	024	102759	39-636-18	0408		3343		1635
13/09/2022	27/09/2022	SEA017	025	102759	39-636-18	0408		3343		1635
28/09/2022	11/10/2022	SEA017	026	102759	39-636-18	0408		3343		1635
12/10/2022	25/10/2022	SEA017	027	102759	39-636-18	0408		3343		1635
26/10/2022	08/11/2022	SEA017	028	102759	39-636-18	0408		3343		1635



Deployment	Recovery	Glider	Mission ID	AD2CP	MINICO2	GPCTD	LEGATO	SBE43F	AROD	METS
09/11/2022	22/11/2022	SEA017	029	102759	39-636-18	0408		3343		1635
23/11/2022	06/12/2022	SEA017	030	102759	39-636-18	0408		3343		1635
07/12/2022	19/12/2022	SEA017	031	102759	39-636-18	0408		3343		1655
20/12/2022	02/01/2023	SEA017	032	102759	39-636-18	0408		3343		1635
03/01/2023	12/01/2023	SEA017	033	102759	39-636-18	0408		3343		1635
13/01/2023	28/01/2023	SEA027	034	102889	42-030-18		210554		59	1635
29/01/2023	08/02/2023	SEA027	035	102889	42-030-18		210554		59	2016
18/02/2023	02/03/2023	SEA017	036	102886	42-030-18		210554		59	2753
03/03/2023	16/03/2023	SEA017	037	102886	42-030-18		210554		59	2753
17/03/2023	30/03/2023	SEA017	038	102886	42-030-18		210554		59	2753
31/03/2023	14/04/2023	SEA017	039	102886	42-030-18		210554		59	2753
15/04/2023	29/04/2023	SEA017	040	102886	42-030-18		210554		59	2753
30/04/2023	14/05/2023	SEA017	041	102886	42-030-18		210554		59	2753
15/05/2023	29/05/2023	SEA017	042	102886	42-030-18		210554		59	2753
30/05/2023	12/06/2023	SEA017	043	102886	42-030-18		210554		59	2753
13/06/2023	26/06/2023	SEA017	044	102886	42-030-18		210554		59	2753
27/06/2023	10/07/2023	SEA017	045	102886	42-030-18		210554		59	2753
11/07/2023	24/07/2023	SEA023	046	103361	42-030-18	0284		2733		2753
28/07/2023	09/08/2023	SEA083	RD8	102880	43-186-18	0408		3489		2821
10/08/2023	24/08/2023	SEA083	RD9	102880	43-186-18	0408		3489		2821
25/08/2023	30/08/2023	SEA083	RD10	102880	43-186-18	0408		3489		2821
26/07/2023	09/08/2023	SEA023	047	103361	42-030-18	0284		2733		2753
12/08/2023	24/08/2023	SEA017	048	103361	42-030-18	0284		2733		2753
25/08/2023	04/09/2023	SEA017	049	103361	42-030-18	0284		2733		2753
30/08/2023	31/08/2023	SEA083	RD11	102280	39-636-18	0408		3489		2821
05/09/2023	12/09/2023	SEA017	050	103361	42-030-18	0284		2733		2753
13/09/2023	16/09/2023	SEA017	051	103361	42-030-18	0284		2733		2753
11/09/2023	16/09/2023	SEA083	RD12	101592	39-636-18	0408		3489		2821
23/09/2023	30/09/2023	SEA017	052	103361	42-030-18	0284		2733		2753
23/09/2023	30/09/2023	SEA083	RD13	101592	39-636-18	0408		3489		2821
02/10/2023	12/10/2023	SEA083	RD14	101592	39-636-18	0408		3489		2821
13/10/2023	01/11/2023	SEA083	RD15	101592	39-636-18	0408		3489		2821
02/11/2023	17/11/2023	SEA083	RD16	101592	39-636-18	0408		3489		2821



Deployment	Recovery	Glider	Mission ID	AD2CP	MINICO2	GPCTD	LEGATO	SBE43F	AROD	METS
18/11/2023	28/11/2023	SEA023	053	102886	42-030-18		210554		59	2821
02/12/2023	15/12/2023	SEA017	054	103361	39-636-18	0284		2733		2821
29/11/2023	02/12/2023	SEA083	RD17	105522	39-636-18	0408		3489		2821
15/12/2023	23/12/2023	SEA083	055	102880	39-636-18	0408		3489		2821
15/12/2023	25/12/2023	SEA027	056	104651	42-030-18	0114		3343		2016
26/12/2023	09/01/2024	SEA027	057	104651	42-030-18	0114		3343		2016
10/01/2024	23/01/2024	SEA027	058	104651	42-030-18	0114		3343		2016
24/01/2024	09/02/2024	SEA027	059	104651	42-030-18	0114		3343		2016
10/02/2024	26/02/2024	SEA027	060	104651	42-030-18	0114		3343		2016
27/02/2024	14/03/2024	SEA027	061	104651	42-030-18	0114		3343		2016
16/03/2024	02/04/2024	SEA027	062	104651	42-030-18	0114		3343		2016

Appendix B

Table B1. Offset and gain values applied to O_2 data depending on profile with reference profiles acquired during MAYOBS cruises.



Profile	Gain
1-4547	1
4548-5349	1.21
5350-7022	1
7023-7796	1.37
7797-8197	1
8198-8389	1.24
8340-13058	1
13059-17884	0.81
17885-19042	1.33
19043-20025	1.22
20026-20240	1
20241-20352	1.10
20353-20635	1
20636-21138	1.36
21139-21450	0.76
21451-21913	1
21914-22047	1.32



Appendix C

Table C1. Sensor information

Parameter	Temperature		Conductivity		Dissolved oxygen		CO_2	CH_4	Ocean currents and BI
Manufacturer	RBR	Seabird	RBR	Seabird	JFE	Seabird	Pro Oceanus	Franatech	Nortek
Sensor	LEGATO	GPCTD	LEGATO	GPCTD	AROD-FT	SBE43F	Mini- CO_2	METS	AD2CP
Unit	$^{\circ}C$		mS/cm		$\mu mol/kg$		$\mu mol/L$	$nmol/L$	-
Range	-5 to +42	-5 to +42	0 to 85	0 to 90	0 to 425	0 to 120% of saturation	0 to 45000	10 to 1000	post-processing
Precision	± 0.002	± 0.005	± 0.003	± 0.003	2% of measurement	2% of saturation	3% of measurement	50	post-processing
Resolution	< 0.00005	0.001	0.001	0.0001	0.01	0.5% of saturation	0.1% of measurement	5	post-processing

Appendix D

Table D1. Percentage of total data going through QC (total number of points for each data is 2,232,706)

Quality flag value	Temperature	Conductivity	Dissolved oxygen	CO_2	CH_4
1 to 4	100%	100%	100%	100%	100%
1 to 3	95.9%	98.2%	99.3%	94.5%	97.1%
1	95.4%	92.4%	84.3%	78.9%	94.7%

Author contributions. All authors except GL took part in data acquisition of the dataset by reviewing the data at two weeks interval since
 375 September 2021. HA was in charge of overall data processing and formatting, with the support of ML, PO and BL. All authors participated
 in the writing of the initial and revised versions of the paper; RE focusing more specifically on the dissolved gases dataset, LP on the ocean
 current dataset and SC on the acoustic backscatter dataset.

Competing interests. The contact author has declared that none of the authors has any competing interests.

Acknowledgements. About data acquisition, we are grateful to REVOSIMA and to the financial support of the French ministries (Ministry of
 380 Overseas, Ministry of the Interior, Ministry of Higher Education, Research and Innovation, Ministry of Ecological Transition and Solidarity).
 We would also like to thank the French oceanographic fleet and the teams deployed on the RV *Marion Dufresne* during the MAYOBS cruises.
 We also thank the technical and piloting teams at Alseamar (Margaux Dufosse and everyone involved in this project) for making the data
 acquisition process as smooth as possible. Without whom nothing would have been possible in Mayotte, we thank the local community for
 allowing us to install a container on the Ballou quay. Last but not least, we would like to thank all those who made it possible for us to



385 deploy, recover and repair the gliders in Mayotte, despite the hazards and often inconvenient timings (Caroline Bachet, Jules Heliou and Mayotteexplo).



References

- Aiken C., Saurel J-M, Foix O. (2021). Earthquake location and detection modeling for a future seafloor observatory along Mayotte's volcanic ridge. *Journal Of Volcanology And Geothermal Research*, 418, 107322 (12p.). <https://doi.org/10.1016/j.jvolgeores.2021.107322>.
- 390 K. L. Deines, "Backscatter estimation using Broadband acoustic Doppler current profilers," Proceedings of the IEEE Sixth Working Conference on Current Measurement (Cat. No.99CH36331), San Diego, CA, USA, 1999, pp. 249-253, 10.1109/CCM.1999.755249.
- de Ruijter, W. P., Ridderinkhof, H., Lutjeharms, J. R., Schouten, M. W., & Veth, C. (2002). Observations of the flow in the Mozambique Channel. *Geophysical Research Letters*, 29(10), 140-1. 10.1029/2001GL013714
- Di Marco, S. F., Chapman, P., Nowlin Jr, W. D., Hacker, P., Donohue, K., Luther, M., ... & Toole, J. (2002). Volume transport and property distributions of the Mozambique Channel. *Deep Sea Research Part II: Topical Studies in Oceanography*, 49(7-8), 1481-1511. 10.1016/S0967-0645(01)00159-X
- 395 Feuillet, N., Jorry, S., Crawford, W. C., Deplus, C., Thinon, I., Jacques, E., ... & Van der Woerd, J. (2021). Birth of a large volcanic edifice offshore Mayotte via lithosphere-scale dyke intrusion. *Nature Geoscience*, 14(10), 787-795. <https://doi.org/10.31223/X5B89P>
- Fiedler, B., Fietzek, P., Vieira, N., Silva, P., Bittig, H. C., & Körtzinger, A. (2013). In situ CO₂ and O₂ measurements on a profiling float. *Journal of atmospheric and oceanic technology*, 30(1), 112-126. <https://doi.org/10.1175/JTECH-D-12-00043.1>
- 400 Fietzek, P., Fiedler, B., Steinhoff, T., & Körtzinger, A. (2014). In situ quality assessment of a novel underwater pCO₂ sensor based on membrane equilibration and NDIR spectrometry. *Journal of Atmospheric and Oceanic Technology*, 31(1), 181-196. <https://doi.org/10.1175/JTECH-D-13-00083.1>
- Francois, R. and Garrison, G. (1982). "Sound absorption based on ocean measurements: Part II: Boric acid contribution and equation for total absorption," *Journal of the Acoustical Society of America*, vol. 72, no. 6, pp. 1879-1890. <https://doi.org/10.1121/1.388673>.
- 405 Garau, B., Ruiz, S., Zhang, W. G., Pascual, A., Heslop, E., Kerfoot, J., & Tintoré, J. (2011). Thermal lag correction on Slocum CTD glider data. *Journal of Atmospheric and Oceanic Technology*, 28(9), 1065-1071. <https://doi.org/10.1175/JTECH-D-10-05030.1>
- Gentil, Mathieu & Many, Gaël & Durrieu de Madron, Xavier & Cauchy, Pierre & Pairaud, Ivane & Testor, Pierre & Verney, Romaric & Bourrin, François. (2020). Glider-Based Active Acoustic Monitoring of Currents and Turbidity in the Coastal Zone. *Remote Sensing*. 12. 10.3390/rs12182875.
- 410 I. Halo, B. Backeberg, P. Penven, I. Ansoerge, C. Reason, J.E. Ullgren, Eddy properties in the Mozambique Channel: A comparison between observations and two numerical ocean circulation models, *Deep Sea Research Part II: Topical Studies in Oceanography*, Volume 100, 2014, Pages 38-53, ISSN 0967-0645, <https://doi.org/10.1016/j.dsr2.2013.10.015>.
- Claudine Hauri, Brita Irving, Dan Hayes, Ehsan Abdi, Jöran Kemme, Nadja Kinski, and Andrew Michael Paul McDonnell, Expanding seawater carbon dioxide and methane measuring capabilities with a Seaglider, Preprint *egusphere-2024-1055*, <https://doi.org/10.5194/egusphere-2024-1055>
- 415 Hedgpeth, J.W. 1957 Treatise on marine ecology and paleoecology. Volume 1, Ecology. The Geological Society of America Memoir 67.
- Heumann Alexandre, Margirier Félix, Rinnert Emmanuel, Lherminier Pascale, Scalabrini Carla, Geli Louis, Pasqueron De Fommervault Orens, Beguery Laurent (2024). 30 months dataset of glider physico-chemical data off Mayotte Island near the Fani Maore volcano. SEANOE. <https://doi.org/10.17882/99960>
- 420 Intergovernmental Oceanographic Commission of UNESCO. 2013.Ocean Data Standards, Vol.3: Recommendation for a Quality Flag Scheme for the Exchange of Oceanographic and Marine Meteorological Data. (IOC Manuals and Guides, 54, Vol. 3.) 12 pp. (English.)(IOC/2013/MG/54-3). <http://dx.doi.org/10.25607/OBP-6>



- Isabelle Leblond, Carla Scalabrin, Laurent Berger. Acoustic monitoring of gas emissions from the seafloor. Part I: quantifying the volumetric
425 flow of bubbles. *Mar Geophys Res* (2014) 35:191–210. 10.1007/s11001-014-9223-y
- Lemoine et al. (2020), The 2018–2019 seismo-volcanic crisis east of Mayotte, Comoros islands: seismicity and ground deformation markers
of an exceptional submarine eruption, *Geophys. J. Int.*, 223(1), 22–44, <https://doi.org/10.1093/gji/ggaa273>
- Lopez-Garcia, P., Hull, T., Thomsen, S., Hahn, J., Queste, B. Y., Krahnmann, G., Williams, C., Woo, M., Pattiaratchi, C., Coppola, L.,
Morales, T., Racapé, V., Gourcuff, C., Allen, J., Alou-Font, E., Zarokanellos, N., Turpin, V., Schmechtig, C., Testor, P., ..., Begler, C.
430 (2022). *OceanGliders Oxygen SOP [Guide]*. OceanGliders. 10.25607/OBP-1756
- Mastin Manon, Cathalot Cecile, Fandino Olivia, Giunta Thomas, Donval Jean-Pierre, Guyader Vivien, Germain Yoan, Scalabrin Carla, Dehez
Sébastien, Jouenne Stéphane, Gaucher Eric C., Rouxel Olivier, Rinnert Emmanuel (2023). Strong geochemical anomalies following active
submarine eruption offshore Mayotte . *Chemical Geology* , 640, 121739 (25p.) . <https://doi.org/10.1016/j.chemgeo.2023.121739>
- Meurer, William & Blum, John & Shipman, Greg. (2021). Volumetric Mapping of Methane Concentrations at the Bush Hill Hydrocarbon
435 Seep, Gulf of Mexico. *Frontiers in Earth Science*. 9. 10.3389/feart.2021.604930.
- Miloshevich, L. M., Paukkunen, A., Vömel, H., & Oltmans, S. J. (2004). Development and validation of a time-lag correction for
Vaisala radiosonde humidity measurements. *Journal of Atmospheric and Oceanic Technology*, 21(9), 1305-1327. [https://doi.org/10.1175/1520-0426\(2004\)021<1305:DAVOAT>2.0.CO;2](https://doi.org/10.1175/1520-0426(2004)021<1305:DAVOAT>2.0.CO;2)
- Miramontes, E., Penven, P., Fierens, R., Droz, L., Toucanne, S., Jorry, S. J., ... & Raison, F. (2019). The influence of bottom currents on
440 the Zambezi Valley morphology (Mozambique Channel, SW Indian Ocean): In situ current observations and hydrodynamic modelling.
Marine Geology, 410, 42-55 10.1016/j.margeo.2019.01.002
- Morison, J., R. Andersen, N. Larson, E. D'Asaro, and T. Boyd, 1994: The correction for thermal-lag effects in Sea-Bird CTD data. *J. Atmos.
Oceanic Technol.*, 11, 1151–1164. [https://doi.org/10.1175/1520-0426\(1994\)011<1151:TCFTLE>2.0.CO;2](https://doi.org/10.1175/1520-0426(1994)011<1151:TCFTLE>2.0.CO;2)
- Mullison, Jerry. (2017). Backscatter Estimation Using Broadband Acoustic Doppler Current Profilers-Updated.
- 445 Ronald S. Oremland, Barrie F. Taylor, Sulfate reduction and methanogenesis in marine sediments, *Geochimica et Cosmochimica Acta*,
Volume 42, Issue 2, 1978, Pages 209-214, [https://doi.org/10.1016/0016-7037\(78\)90133-3](https://doi.org/10.1016/0016-7037(78)90133-3)
- Owens, W. B., & Millard Jr, R. C. (1985). A new algorithm for CTD oxygen calibration. *Journal of Physical Oceanography*, 15(5), 621-631.
- Pasqueron de Fommervault, O. Besson, F., Lattes, P. (2018). SeaExplorer Underwater Glider: A New Tool to Measure Water Velocity. *Marine
Technology* 42, 44-47. 10.1109/OCEANSE.2019.8867228
- 450 Pouliquen Sylvie, Petit De La Villeon Loic, Carval Thierry (2011). *Argo Data Management : contribution to Marine Climate Data System
(MCDS) workshop* . IDM/ISI/11-070 .
- C. Schmechtig, V. Thierry, The Bio Argo Team Argo Quality Control Manual for Biogeochemical Data. *The Bio Argo* (2016),
10.13155/40879.
- Stommel, H. 1989. The Slocum Mission. *Oceanography* 2(1):22–25, <https://doi.org/10.5670/oceanog.1989.26>.
- 455 Testor, Pierre & Meyers, Gary & Pattiaratchi, Charitha & Bachmayer, Ralf & Hayes, D. & Pouliquen, Sylvie & Villeon, Loic & Carval,
Thierry & Ganachaud, Alexandre & Gourdeau, Lionel & Mortier, Laurent & Claustre, Hervé & Taillandier, Vincent & Lherminier,
Pascale & Terre, T. & Visbeck, Martin & Karstensen, Johannes & Krahnmann, Gerd & Alvarez, A. & Owens, Breck. (2010). Gliders as
a Component of Future Observing Systems. *Proceedings of OceanObs'09: Sustained Ocean. Observations and Information for Society*
.Hall, J., Harrison, D.E. & Stammer, D., Eds., ESA Publication WPP-306,. 2. 10.5270/OceanObs09.cwp.89



- 460 Gregor Rehder, Ira Leifer, Peter G. Brewer, Gernot Friederich, Edward T. Peltzer. Controls on methane bubble dissolution inside and outside the hydrate stability field from open ocean field experiments and numerical modeling. *Marine Chemistry* 114 (2009) 19–30 <https://doi.org/10.1016/j.marchem.2009.03.004>
- Robert E. Todd, Francisco Chavez, Sophie Clayton, Sophie Cravatte, Marlos Goes, et al.. Global Perspectives on Observing Ocean Boundary Current Systems. *Frontiers in Marine Science*, Frontiers Media, 2019, 6, <https://doi.org/10.3389/fmars.2019.00423>
- 465 Russell-Cargill Louise M., Craddock Bradley S., Dinsdale Ross B., Doran Jacqueline G., Hunt Ben N., Hollings Ben (2018) Using autonomous underwater gliders for geochemical exploration surveys. *The APPEA Journal* 58, 367-380. <https://doi.org/10.1071/AJ17079>
- Van Haren, H., and L. Gostiaux (2010), A deep-ocean Kelvin-Helmholtz billow train, *Geophys. Res. Lett.*, 37, L03605, doi:10.1029/2009GL041890.
- Visbeck, M. (2002). Deep velocity profiling using lowered acoustic Doppler current profilers: Bottom track and inverse solutions. *Journal of atmospheric and oceanic technology*, 19(5), 794-807. [https://doi.org/10.1175/1520-0426\(2002\)019<0794:DVPULA>2.0.CO;2](https://doi.org/10.1175/1520-0426(2002)019<0794:DVPULA>2.0.CO;2)
- 470 Wyrski, K. (1971) *Oceanographic Atlas of the International Indian Ocean Expedition*. National Science Foundation, Washington DC.
- Zinke et al. (2003), Postglacial flooding history of Mayotte Lagoon (Comoro Archipelago, southwest Indian Ocean). *Marine Geology*, 194(3–4), 181–196. [https://doi.org/10.1016/S0025-3227\(02\)00705-3](https://doi.org/10.1016/S0025-3227(02)00705-3)
- Zinke et al. (2005), Facies and faunal assemblage changes in response to the Holocene transgression in the Holocene transgression in the
- 475 Lagoon of Mayotte (Comoro Archipelago, SW Indian Ocean). *Facies* 50 :391–408 [10.1007/s10347-004-0040-7](https://doi.org/10.1007/s10347-004-0040-7)